Korean J. Chem. Eng., 38(8), 1686-1702 (2021)
DOI: 10.1007/s11814-021-0795-3

pISSN: 0256-1115
eISSN: 1975-7220

Combination of inertial focusing and magnetoporetic separation in a novel microdevice

Afshin Shiriny, Morteza Bayareh†, and Afshin Ahmadi Nadooshan

Department of Mechanical Engineering, Shahrekord University, Shahrekord, Iran
(*Received 1 February 2021 • Revised 27 March 2021 • Accepted 28 March 2021*)

Abstract−Separation of microparticles is of great importance in diagnostic, chemical, and biological analysis, as well as food processing and environmental assessments. In the present work, a novel microfluidic device is designed to focus microparticles based on inertial and magnetophoretic impacts. Three permanent magnets are mounted in the vicinity of the microchannel to separate the diamagnetic particles suspended in a ferrofluid by applying a negative magnetophoretic force. Polystyrene particles with three sizes of 5, 10, and 15 μm are separated from each other using the proposed device with 100% separation efficiency. The results show that high purity of particle collection can be achieved using Halbach array of magnets at Reynolds numbers of 100 and 110. The influence of inlet flow velocity, magnets' configuration, and their distance from the microchannel is investigated and the optimal situations are determined.

Keywords: Microfluidic, Inertial Separation, Spiral Microchannel, Magnetoforsis, Permanent Magnet

INTRODUCTION

Microfluidics is a rapidly growing interdisciplinary field of numerical and experimental investigations. On the other hand, the separation of microparticles has great importance in chemical and biological analyses, food processing, and environmental assessment. Microfluidic devices can separate and sort different micron-sized particles, cells, and droplets [1].

Particle separation is by active and passive techniques. Passive methods use the interaction between particles, the microchannel structure, and the fluid flow field to separate the particles. These methods do not depend on external forces, but their operational range is small due to their geometry and design [2]. The most important passive methods are microfiltration [3], deterministic lateral displacement (DLD) [4], pinched flow fractionation (PFF) [5], and inertial force and Dean flow [6]. In the active methods, an external field such as electric, magnetic, optical, and acoustic is employed to separate the particles. Active methods have more control over the separation process, can be set up in real time and are more reliable. The separation power and efficiency of active methods are higher than those of passive ones [2]. The most important active separation methods are dielectrophoresis [7], acoustophoresis [8], and magnetophoresis [9].

1. Inertial Separation

In inertial focusing, suspended particles within a fluid flow can migrate across streamlines and be sorted at specific equilibrium locations in the cross section of the channel. This behavior occurs as a result of inertial forces and can be adjusted by channel geometry and flow conditions [10]. In straight channels, inertial focusing occurs due to the balance between two dominant forces: i) shear gradient inertial lift force ($\mathbf{F}_{SL}$) due to the curvature of the fluid velocity profile and ii) wall induced inertial lift force ($\mathbf{F}_{WL}$) due to the interaction between the particle and the adjacent wall. $\mathbf{F}_{SL}$ pushes the particles towards the channel walls, while $\mathbf{F}_{WL}$ moves them from the walls to the channel center [11]. Therefore, particles tend to obtain an equilibrium position due to force balance. The magnitude of the net inertial lift force $\mathbf{F}_L$ is a function of its magnitude for different particles. The pattern of particle separation in straight channels depends on the geometry of the channel. In a channel with a circular cross-section, particles are concentrated close to a ring with a radius of 0.6 times the channel radius [11]. In square and rectangular channels with an aspect ratio close to 1, the particles are concentrated on four points close to the midpoint of the walls [12]. For rectangular channels with an aspect ratio much larger than 1 or much smaller than 1, the particle equilibrium position is reduced to two positions near the midpoint of the larger walls of the channel [13]. In curved channels, the particles flowing in the fluid withstand a centrifugal force in the radial direction. This force causes the formation of two opposite vortices called Dean vortices in the upper and lower half of the channel. Dean vertices produce a secondary flow or Dean flow in the cross section of the channel perpendicular to the mainstream. Dean flow occurs as a result of a difference in the velocity across the channel, leading to a drag force called Dean drag force $\mathbf{F}_D$, which is proportional to the particle size [14]. The direction of the Dean drag force is towards the outer radius of the channel [11]. $\mathbf{F}_L$ acts in the direction of $\mathbf{F}_D$ in the vicinity of the outer wall of the channel, so that the particles move along the Dean vortices regardless of their size. Close to the inner channel wall, $\mathbf{F}_L$ and $\mathbf{F}_D$ act in opposite directions. Thus, the particles either concentrate in an equilibrium position or continue to rotate along with the Dean vortices, depending on the magnitude of these forces. Since the number of equilibrium positions of particles can be reduced to one position, Dean flow allows the particles to separate based on their size [14].

†To whom correspondence should be addressed.
E-mail: m.bayareh@sku.ac.ir
Copyright by The Korean Institute of Chemical Engineers.

Particle separation using inertial force has been studied numerically and experimentally by many researchers. The type of particles, their size, and microchannel geometry are the items whose effect on particle separation efficiency has been investigated. Abdulla et al. [9] used a microfluidic device consisting of two five-loop helical microchannels and a zigzag microchannel to separate two types of CTCs (lung cancer cells with an average diameter of 15 μm and breast cancer cells with an average diameter of 24 μm) from white and red blood cells and reached a separation efficiency of 80.75% for lung cancer cells and 73.75% for breast cancer cells. Bhagat et al. [15] separated the 1.9 and 7.32 μm polystyrene particles suspended in the water using a five-loop spiral microchannel. According to their results, complete separation of particles occurs at the inlet flow rate of 20 ml/h (Re=5). In an experimental study, Al-Halhouli et al. [16] separated 2- and 5-μm as well as 2- and 10-μm polystyrene particles suspended in the water using a nine-loop spiral microchannel with a trapezoidal cross section. Sun et al. [17] experimentally isolated two types of CTCs (cervical cancer cells of 13 μm in diameter and breast cancer cells of 18 μm in diameter) from blood cells using two spiral microchannels with six clockwise and six counterclockwise loops. They reached the highest collection rate of 96.77% for CTCs and 92.28% for blood cells at an inlet flow rate of 20 ml/min. Yeh et al. [18] achieved separation efficiency of 99.7% and 98.3% for polystyrene particles of 1 and 5.5 μm, respectively, suspended in water using a four-loop spiral microchannel. The optimal inlet flow rate was reported to be 0.4 ml/min. Rzhevskiy et al. [19] isolated prostate cancer cells with an average diameter of 15 to 30 μm from urine using a five-loop spiral microchannel and achieved a separation efficiency of 86%.

2. Magnetophoretic Separation

Magnetophoresis is the phenomenon by which particles migrate in a magnetic field and can be divided into two categories: positive and negative magnetophoresis. Positive magnetophoresis is the motion of magnetic particles in a diamagnetic medium, and negative magnetophoresis is the migration of diamagnetic particles in a magnetic medium. Magnetophoresis occurs when there is either a magnetic field gradient or an ambient magnetization gradient, or a combination of both. This technique does not affect the solution properties, including pH, ion concentration, surface charge, and temperature. Besides, this separation method is easy to apply and cheap. It is also non-invasive due to indirect contact of the magnetic source with the test sample. Key parameters for design and optimization using magnetophoresis are magnetic permeability (μ_r), magnetic flux density (**B**), and magnetism (χ). The negative magnetophoretic force is proportional to the volume of the particle, so the particles can be separated from each other based on their size [20]. Negative magnetophoresis has attracted considerable attention in recent years in the field of disease diagnosis, treatment studies, concentration, and cell separation. Munaz et al. [21] designed a three-dimensional microfluidic device for the magnetophoretic separation of diamagnetic particles using two-stream and three-stream ferrofluid configurations. They reported that the highest separation efficiency corresponded to the three-stream structure in which the ratio of the sheath flow to sample one was equal to 1.5 : 1 : 1.5. The efficiency for 3.2- and 4.8-μm particles was 78 and 75%, respectively. Zhu et al. [22] designed a magnetophoresis-based microfluidic device to separate 1- and 7.3-μm polystyrenes in a continuous ferrofluid flow. They employed a Y-shaped microchannel and reached a separation efficiency of 100%. In an experimental study, Zhang et al. [23] proposed a new microfluidic device for the magnetophoretic separation of 5- and 13-μm microparticles in a continuous magnetic fluid flow using a permanent magnet. They obtained the purity of 99.3% and 90.8% for 5- and 13-μm microparticles, respectively. Zhao et al. [24] used a bio-compatible ferrofluid to isolate cancer cells without the need for labeling of white blood cells. Two types of lung cancer cells with diameters of 15.5 and 16.9 μm, two kinds of breast cancer cells with diameters of 18.1 and 18.7 μm and a type of prostate cancer cells with an average diameter of 18.9 μm were separated by their proposed microchannel with the efficiency of 80, 81, 82, 82, and 86%, respectively. Wu et al. [25] investigated the separation of diamagnetic microparticles suspended in a ferrofluid using two different arrangements of permanent magnets near the microchannel. Their proposed microchannel consisted of two straight channels with a rectangular cross section. They reported that the deflection angle of the particles is larger for the Halbach array of magnets. Using a single-loop microchannel in the vicinity of an array of 30 permanent magnets, Xue et al. [26] separated cancer cells and white blood cells by applying the magnetophoretic field. Their proposed microchannel consisted of a loop with two inlets for injecting sample and buffer streams and two outlets for isolating the cells.

As pointed out in the literature, previous researchers have employed passive microfluidic devices with multiple loops to isolate microparticles or CTCs. In the present work, inertial and magnetophoretic forces are employed to separate three sizes of diamagnetic microchannels suspended in a ferrofluid using a single-loop channel. The microchip proposed in this article is very easily industrially fabricated. To the best of our knowledge, this geometry is the first one to use a single loop to separate microparticles where a Halbach array of magnets is employed. Magnetophoretic separation requires low flow velocity for sufficient particle residence time, while effective inertial separation needs high flow velocity. The main objectives of the present study were to introduce a simple microfluidic device and achieve optimal boundary conditions in which the separation efficiency is maximum.

THEORY

In this research, the separation of diamagnetic particles suspended in a ferrofluid is investigated using the combined effects of inertial and magnetophoretic forces. The schematic of the problem is shown in Fig. 1. The microchannel consists of a curved channel, i.e., spiral section, for inertial separation and a straight section for magnetophoretic separation of particles. The two parts are connected by an interface channel called the expansion region. The curved part has a loop with a rectangular cross section and consists of two inlets for sample flow and sheath flow. The ferrofluid flow containing three samples of diamagnetic particles with different diameters is injected into the external inlet. Ferrofluid is also injected into the internal inlet to create a compressed flow near the outer wall of the channel [19]. The width of the channel in the curved part is 500 μm, its height is 200 μm, and the radius of the channel curvature

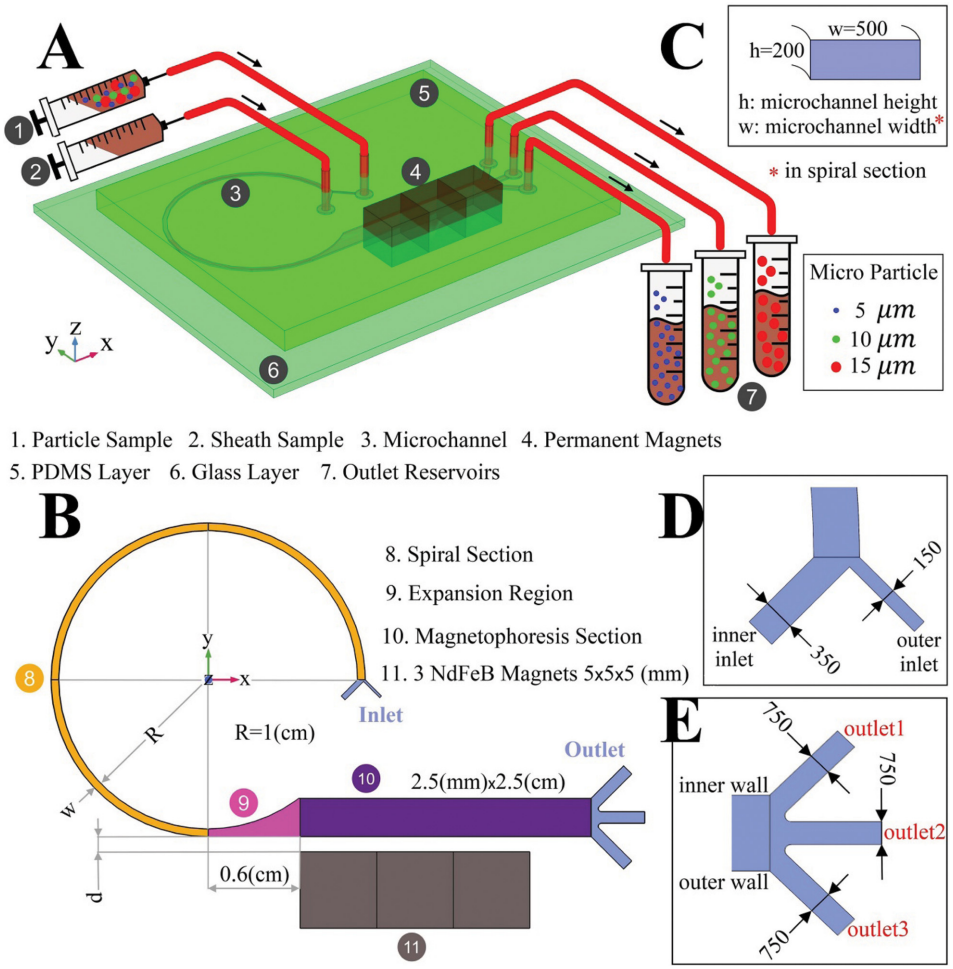


Fig. 1. Schematic of the problem: (A) overview of the designed microchip, (B) microchannel geometry, (C) microchannel cross section, (D) microchannel inlet, and (E) microchannel outlet (all dimensions are in micrometers).

is 1 cm. The large size of the channel eliminates particle clogging within the microchannel [2]. The second part consists of a straight rectangular channel with a width of 2.5 mm, a height of 200 μm, and a length of 2.5 cm. Three permanent neodymium magnets with dimensions of 5×5×5 mm are placed close to the outer wall of the magnetophoretic section with a distance of d. In the following, the theory and relations related to the inertial and magnetophoretic separation of particles are presented.

The fluid flowing in the curved channel experiences a centrifugal acceleration in the radial direction towards the outer radius of the channel, leading to the formation of two vortices, i.e., Dean vortices, in the top and bottom halves of the channel. The magnitude of these secondary flows is quantified using a dimensionless number called Dean number (De) [9]:

$$De=\frac{\rho U D_h}{\mu}\sqrt{\frac{D_h}{2R}}=Re\sqrt{\frac{D_h}{2R}} \tag{1}$$

where ρ, μ and U are the density, dynamic viscosity, and average velocity of the fluid, respectively. D_h represents the hydraulic diameter and R is the radius of channel curvature. For a channel with a rectangular cross section, $D_h=2wh/(w+h)$, where w is the channel width and h is the channel height. $Re=\rho UD_h/\mu$ represents the Reynolds number. In the magnetophoretic section, the Dean number is zero, and therefore the Dean vortices are not formed.

In the curved channel, the Dean number increases with the Reynolds number, the curvature, and the hydraulic diameter. Ookawara et al. [27] provided a relation to calculate the maximum Dean velocity:

$$U_D=1.8\times10^{-4}\,De^{1.63}\ (m/s) \tag{2}$$

Buoyant particles in a fluid withstand a force called the hydrodynamic drag force that acts against the fluid flow directions. This force can be calculated according to Stokes' law [28]:

$$\mathbf{F}_D=3\pi a\mu(\mathbf{u}_f-\mathbf{u}_p)f_D \tag{3}$$

where a represents the diameter of the particles. Also, $\mathbf{u}_f$ and $\mathbf{u}_p$ are the velocity of the fluid and the particle, respectively. f_D, which is called the drag coefficient, indicates the wall effects and can be calculated as follows [28]:

$$f_d=\left[1-\frac{9}{16}\alpha+\frac{1}{8}\alpha^3-\frac{45}{256}\alpha^4-\frac{1}{16}\alpha^5\right]^{-1} \tag{4}$$

where $\alpha=r_p/(r_p+L)$, r_p is the radius of the particle, and L is the distance from the particle to the nearest wall. Note that in the spiral section of the microchannel, the Dean drag force is exerted on the

particles, which is assumed to be $F_D=3\pi\mu aU_D$ [29]. The Stokes flow assumption is valid because the microfluidic devices operate in the laminar flow regime (1<Re<100) [73]. This drag force causes the particles to move along the Dean vortices, moving towards the inner or outer wall of the channel. In addition to the drag force, the suspended particles also withstand inertial lift forces due to shear gradients and wall effects. In Poiseuille flow, the net lift force applied to the particles is [30]:

$$\mathbf{F}_L=\frac{\rho U_m^2 a^4}{D_h^2}\mathbf{f}_L \tag{5}$$

where U_m=2U [9] is the maximum fluid velocity and $\mathbf{f}_L=\mathbf{f}_L(Re_c, \mathbf{x}_p)$ is the lift coefficient. Re_c and $\mathbf{x}_p$ are channel Reynolds number that is defined based on U_m and particle position in channel cross section, respectively. For channels with rectangular cross section, the lift coefficient is in the range of 0.2-0.5 at Re<100 [30]. As mentioned, the inertial lift force pushes particles near the wall towards the channel center and particles near the center area towards the channel walls. The competition between the drag force and inertial lift force determines the equilibrium position of each particle, depending on its size [31]. When a particle migrates from the vicinity of the channel wall towards the opposite wall and then returns to the original wall, a Dean cycle is formed. For a channel with a rectangular cross section, the length of a Dean cycle is l_{DC}=2w+h [16]. To describe the trajectory of particles in a channel, the particle Reynolds number is defined as $Re_p=Re_c(a/h)^2$ [32]. Inertial focusing requires Re_p>1 and a/h>0.07 [33]. Thus, when the inertial lift force overcomes the drag force, larger particles migrate towards the inner channel wall, while smaller particles move along the Dean vortices.

The magnetophoretic separation of microparticles includes a coupled electromagnetic, fluid, and particle dynamics problem [34]. To generate the magnetic field, the Maxwell equation should be solved [35]:

$$\mathbf{H}=-\nabla V_m \tag{6}$$

where **H** is the magnetic field strength and V_m is the scalar magnetic potential. The Gauss equation is also solved for magnetic flux density **B** [36]:

$$\nabla\cdot\mathbf{B}=0 \tag{7}$$

Eq. (8) describes the magnetization relation for the magnet blocks and Eq. (9) represents the relative permeability employed otherwise [36]:

$$\mathbf{B}=\mu_0(\mathbf{H}+\mathbf{M}) \tag{8}$$

$$\mathbf{B}=\mu_0\mu_r\mathbf{H} \tag{9}$$

where $\mu_0=4\pi\times10^{-7}$ (T·m/A) is the air permeability coefficient, μ_r is the relative magnetic permeability of the fluid, and **M**(A/m) is the magnetization of the magnet. μ_r can be calculated as follows [36]:

$$\mu_r=1+\chi \tag{10}$$

where χ is the magnetism of matter. The dominant forces in the straight section of the microchannel are the hydrodynamic drag force and magnetophoretic one. The magnetophoretic force for the fluids when microparticle concentration is less than 1% [37] is as follows:

$$\mathbf{F}_M=2\pi r_p^3\mu_0\mu_{r,f}K\nabla\mathbf{H}^2 \tag{11}$$

$$K=\frac{\mu_{r,p}-\mu_{r,f}}{\mu_{r,p}+2\mu_{r,f}} \tag{12}$$

where $\mu_{r,f}$ and $\mu_{r,p}$ represent the relative magnetic permeability of the fluid and the particle, respectively.

Since the fluid is Newtonian and incompressible and the fluid flow is assumed to be laminar and single phase, the governing equations are continuity and Navier-Stokes equations:

$$\rho\nabla\cdot\mathbf{u}_f=0 \tag{13}$$

$$\rho(\mathbf{u}_f\cdot\nabla)\mathbf{u}_f=\nabla\cdot[-p\mathbf{I}+\mu(\nabla\mathbf{u}_f+(\nabla\mathbf{u}_f)^T)] \tag{14}$$

where $\mathbf{u}_f$ indicates the fluid velocity and p is the fluid pressure. The properties of the magnetic fluid used in this study are derived from the experimental data of Zhou et al. [38]: μ=0.0105 Pa·s, ρ= 1,070 Kg/m^3, and $\mu_{r,f}$=1.025. Also, diamagnetic polystyrene particles with three different diameters of 5, 10, and 15 μm were used in the present simulations. The particle density is assumed to be 1,050 Kg/m^3 and $\mu_{r,p}$=1. From the experimental work of Chen et al. [39], the relative magnetism of magnets is set to one and their magnetization is M=9.9×10^5 A/m. The ratio of the sample flow rate to the sheath flow rate is set to 1 : 19. The inlet Reynolds number is in the range of 70-120. No-slip boundary condition is employed for the microchannel walls and zero-pressure boundary condition is used for the outlets. The inlet velocity boundary condition is applied to the inlets. According to the desired inflow ratio, the velocity in the inner and outer inlets is equal to 0.95Q and 0.05Q, respectively, where Q is the total mass flow rate.

Three-dimensional simulations were performed using COMSOL Multiphysics 5.5 software. Navier-Stokes equations were solved using the finite element method and P2+P2 scheme was selected to discretize the velocity and pressure. The P2+P2 method considers the second-order derivative of the fluid velocity components [40]. To track the location of particles, Newton's second law of motion is employed:

$$\frac{d}{dt}(m_p\mathbf{u}_p)=\mathbf{F}_D+\mathbf{F}_L+\mathbf{F}_M \tag{15}$$

where m_p and $\mathbf{u}_p$ are the mass and velocity of the particles, respectively.

The time-dependent solution was performed using an Eulerian method. The solution of laminar flow was used as the input velocity to track the position of the particles. 80 particles with a diameter of 5 μm, 80 particles with a diameter of 10 μm, and 80 particles with a diameter of 15 μm were injected into the microchannel through the outer inlet of the microchannel with a velocity equal to the velocity of the ferrofluid flow. A drag force calculated based on Stokes' law was applied on the particles. A correction factor was induced for the drag force for the particles placed in the vicinity of walls. A time step was assumed to be 1 ms, and the relative tolerance convergence criterion was 10^{-5}. Each model was solved using the generalized minimal residual (GMRES) iterative solver.

VALIDATION

The present simulations were compared with some numerical and experimental results. First, the present work was compared with the experimental data presented by Bhagat et al. [12] who employed a five-loop spiral microchannel with a rectangular cross-section of 50×100 μm and two inlets for injection of sample flow and sheath flow. The first spiral radius was 3 mm and the distance between two consecutive loops was 250 μm. 100 polystyrene particles with diameters of 7.32 and 1.9 μm suspended in water were injected into the outer inlet and water was injected into the inner inlet as sheath flow. The inlet flow rate was 10 μl/min. At the spiral outlet, two branches were provided to separate the particles so that the large particles exited from the inner outlet and small ones passed through the outer outlet. Fig. 2 demonstrates the distribution of particles at the microchannel outlet, indicating good agreement between the present results and the experimental ones.

For further validation, the present numerical results were compared with the experimental work of Hou et al. [41] who used a microchannel consisting of an internal semicircle with a radius of R_1=0.42 cm and an external spiral loop with a radius of R_2=(1.0+0.1$\theta/2\pi$) cm with two inlets and two outlets of a rectangular cross section (500 μm×155 μm). 200 polystyrene particles with diameters of 6 μm and 15 μm suspended in water were injected into an inlet and pure water was injected into the second inlet as sheath flow. The ratio of the flow containing particles to the sheath flow was considered to be 1 : 9. Fig. 3 compares the maximum Dean velocity for different inlet Reynolds numbers achieved by the present simulations and the ones reported by Hou et al. [41] and calculated by Eq. (2), showing that the current results are in excellent agreement with the numerical data. Also, in Fig. 4, the equilibrium position width of 6- and 15-μm particles across the channel outlet cross section is presented for different Dean cycles at Re=5. As can be seen, the equilibrium position of 6- and 15-μm particles is in the vicinity of the inner and outer channel walls, respectively.

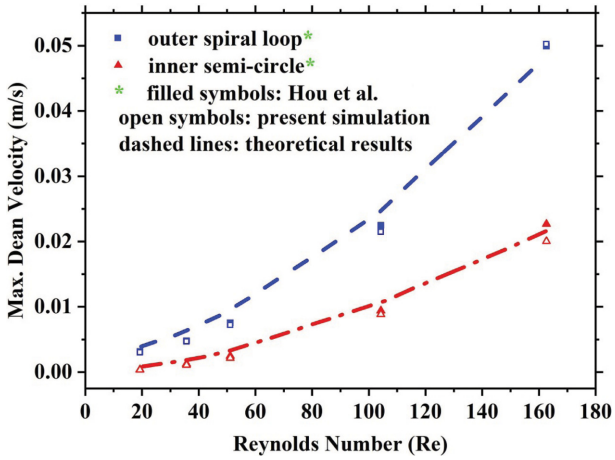


Fig. 3. Maximum Dean velocity at the microchannel cross section obtained from the present simulations compared to the ones reported by Hou et al. [41] and analytical results of Ookawara et al. [27].

To validate the magnetophoretic effect, the present results were

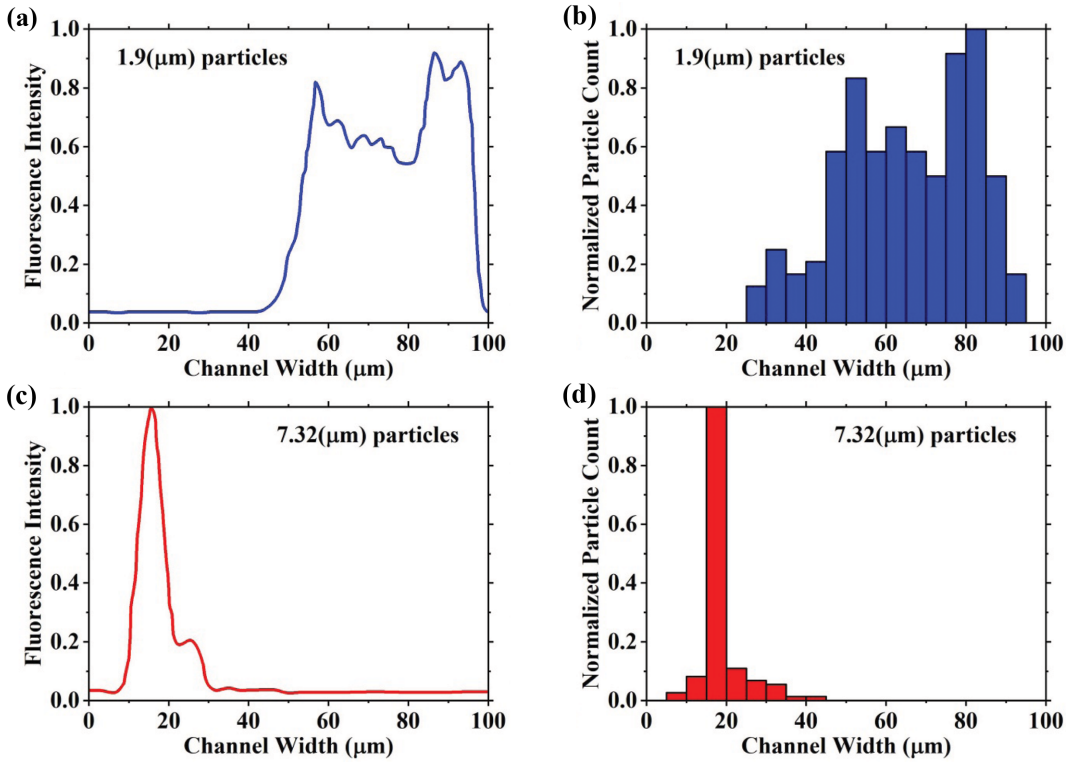


Fig. 2. Distribution of 7.32- and 1.9-μm particles at the spiral microchannel outlet section: (a) and (c) experimental results correspond to 1.9- and 7.32-μm particles, respectively, and (b) and (d) the present results for 1.9- and 7.32-μm particles, respectively.

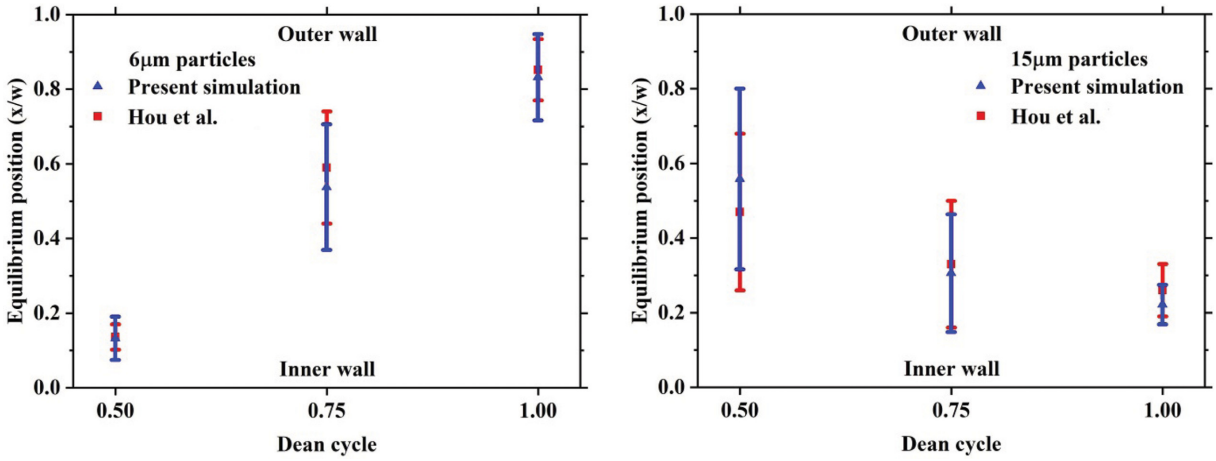


Fig. 4. Equilibrium position width of 15-μm (right) and 6-μm (left) particles for different Dean cycles.

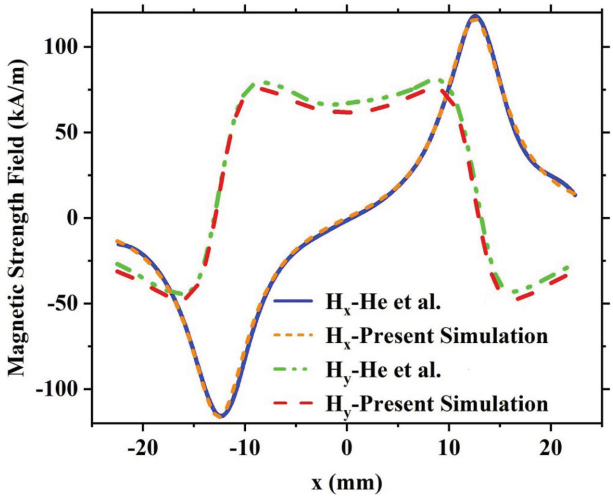


Fig. 5. Magnetic field strength along the channel centerline.

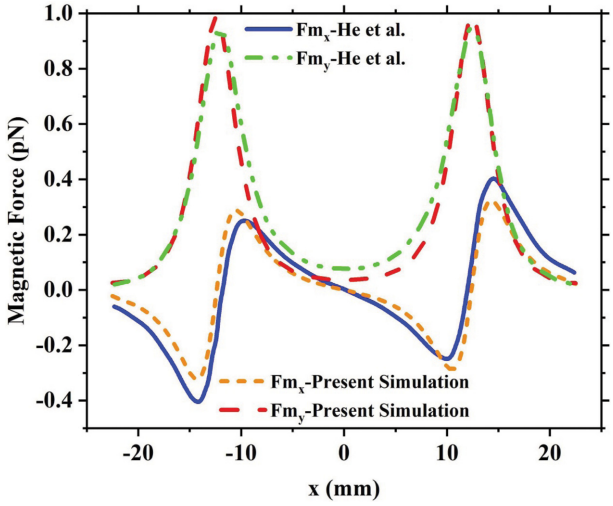


Fig. 6. Magnetophoretic force along the channel center line.

compared with the ones reported by He et al. [42] in Figs. 5 and 6. A microchannel with rectangular cross section (45×1 mm) containing ferrofluid with a density of 1,100 Kg/m^3, a viscosity of 0.002 Pa·s, relative magnetism of 1.063, and a flow rate of 50 μl/min was considered. A permanent magnet (25×3 mm) with a relative magnetism of 1.05 and a residual flux density of 250 mT was also used. Fig. 5 shows the magnetic field strength **H** in terms of channel length on the centerline of a straight microchannel containing diamagnetic microparticles suspended in a magnetic fluid exposed to a non-uniform magnetic field. Also the distribution of negative magnetophoretic force in the flow direction ($\mathbf{F}_{mx}$) and perpendicular to it ($\mathbf{F}_{my}$) was compared, indicating good agreement with the reference results.

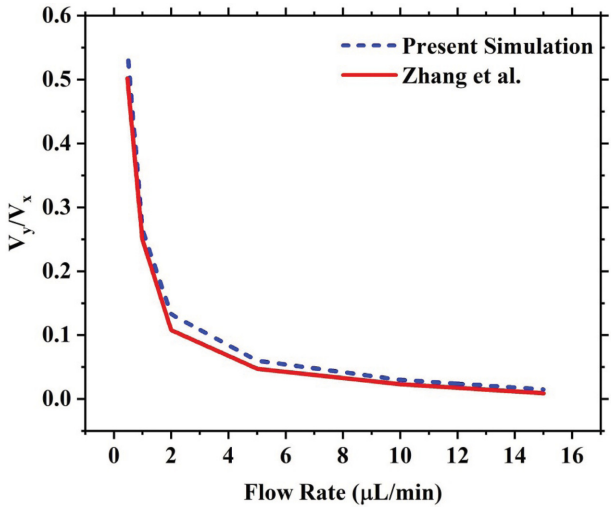


Fig. 7. The ratio of lateral velocity to horizontal velocity of microparticles for different inlet flow rates.

For another validation, negative magnetophoretic deflection of diamagnetic microparticles in a straight microchannel exposed to a permanent magnet was simulated and compared with the experimental results of Zhang et al. [23]. Fig. 7 illustrates the ratio of lateral velocity to horizontal velocity of 5-μm particles in a two-dimensional microchannel with a width of 600 μm and a length of 7,200 μm. A 4×4 mm magnet with a relative magnetism of 1.05 and a residual flux density of 120 mT is located at a 1-mm distance from

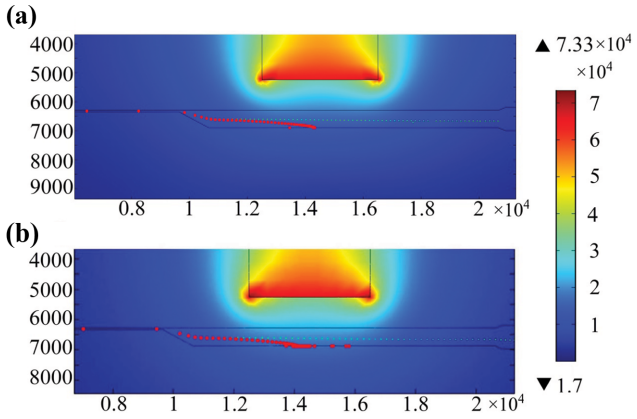


Fig. 8. Magnetophoretic separation of 5- and 13-μm polystyrene particles suspended in a ferrofluid (color contours indicate the intensity of the magnetic field): (a) The present work; (b) the reference results [23].

Table 1. The present results for grid-independence test

Number of elements	$U_{Dean,max}$ (mm/s)	$H_{max}/10^5$ (A/m)
382829	5.0513	9.8
764212	5.0516	9.83
2104678	5.0522	9.9
7525818	5.0531	10.1
7742417	5.0531	10.1

the channel. The density of the fluid is 1,007 Kg/m^3, its viscosity is 0.008 Pa·s, and its relative magnetism is set to 1.063. Also, in Fig. 8, numerical simulation of magnetophoretic separation of 5- and 13-μm particles is compared with the numerical results of Ref. [23]. The microchannel consists of three inlets with rectangular cross sections of 20 mm×50 μm, 10 mm×600 μm, and 5 mm×800 μm. The inlet flow rate is 2 μl/min. The distribution of the magnetic field strength is shown in Fig. 8, indicating good agreement between the present results and the reference ones.

GRID STUDY

Five grid resolutions of 382829, 764212, 2104678, 7525818, and 7742417 with tetrahedral mesh elements were considered for the grid-independence test. For each case, the governing equations were solved to obtain $U_{Dean,max}$ and H_{max}. Table 1 presents the magnitude of $U_{Dean,max}$ in the cross section of the spiral section and H_{max} within the microchannel for five different meshes. As can be seen, the results for the grid with 7742417 elements are the same as the ones for the grid resolution of 7525818. Therefore, the grid resolution of 7525818 is used for further simulations. A schematic of the grid is presented in Fig. 9.

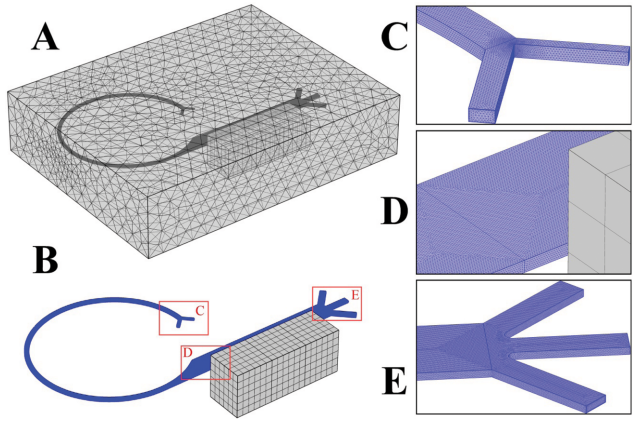


Fig. 9. Schematic of the grid used in the present simulations.

RESULTS AND DISCUSSION

1. The Effect of Reynolds Number

In this section, the effect of inlet flow velocity on particle separation is studied. The simulations were performed for different Reynolds numbers, ranging from 70 to120 corresponding to the flow rate of 86.5 and 148.4 ml/h. Note that the flow rate is the total inlet flow rate in the spiral section of the microchannel. Table 2 compares the different values of the velocity obtained from the simulations and the theoretical equations, showing that there is a good agreement between the results. Fig. 10 demonstrates the Dean flow velocity contours across the channel for different Reynolds numbers. By adding curvature to the straight channel, it is expected that the fluid velocity near the outer wall of the channel becomes greater than that near the inner wall, because the fluid travels a longer distance in the vicinity of the outer wall. This difference in the velocity causes a secondary flow and motion of the fluid from the inner wall towards the outer wall of the channel, leading to the formation of Dean vortices. However, to maintain fluid continu-

Table 2. The values of Dean velocity and maximum velocity for different Dean and Reynolds numbers

Re	Q (ml/h)	De	Theoretical U_D (mm/s)	Simulation U_D (mm/s)	Theoretical U_m (m/s)	Simulation U_m (m/s)	Theoretical U_m (m/s)	Simulation U_m (m/s)
			Spiral section		Spiral section		Straight section	
70	86.5	8.4	5.7	5.3	0.48	0.46	0.09	0.08
80	99.0	9.6	7.1	6.6	0.55	0.52	0.10	0.09
90	111.3	10.8	8.6	8.1	0.62	0.59	0.12	0.10
100	123.6	12.0	10.3	10.1	0.69	0.65	0.14	0.11
110	136.0	13.2	12.0	12.2	0.76	0.72	0.15	0.12
120	148.4	14.3	13.8	14.5	0.82	0.78	0.16	0.13

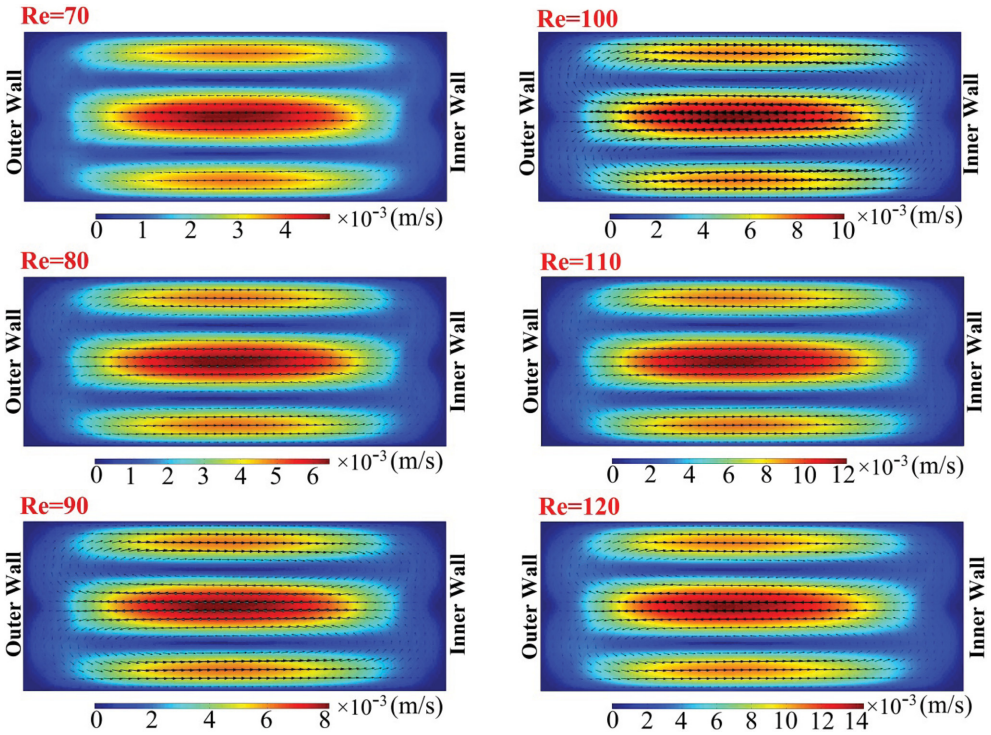


Fig. 10. Dean flow in the proposed microchannel: Lateral velocity contours at the microchannel cross section for six different Reynolds numbers. The arrows show that the cross-sectional pattern of Dean flow is well developed. The color bar gives the Dean velocity.

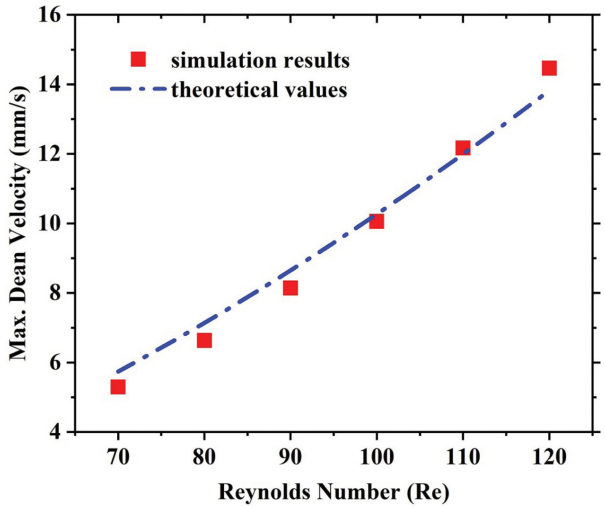


Fig. 11. Maximum Dean flow velocity for different Reynolds numbers.

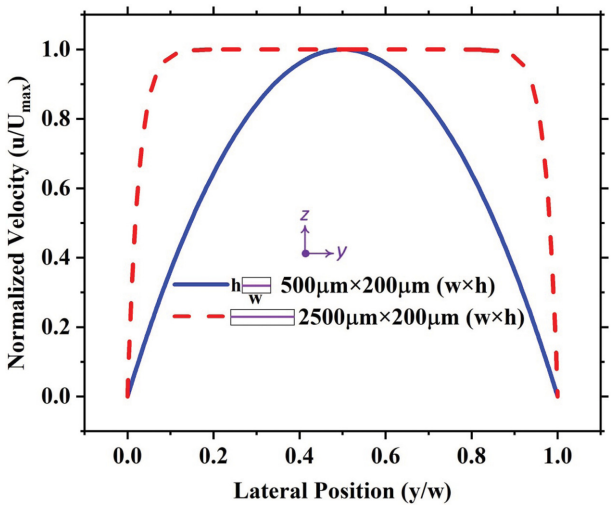


Fig. 12. Normalized velocity across the microchannel for spiral and straight sections.

ity, this circulation continues and leads to the development of the Dean flow across the channel cross section. As can be seen in this figure, Dean flow in the channel has been developed. Also, according to previous studies, the direction of Dean flow is towards the outer channel curvature in the central region of the channel and is in the direction of the channel curvature at its top and bottom walls.

Fig. 11 shows the maximum velocity of Dean flow for different Reynolds numbers. It is revealed that the present results are in good agreement with the results of Eq. (2) reported by Ookawara et al. [27]. The maximum values of the secondary flow velocity in the curved section of the microchannel are obtained by Eq. (2) and simulations. As the Reynolds number increases, the Dean number increases according to Eq. (1), and consequently, the Dean flow velocity in the microchannel cross-section is enhanced (Eq. (2)).

Fig. 12 illustrates the velocity profile normalized with the maximum velocity at the line passing through the microchannel center in spiral and straight sections. The mainstream velocity profile in the microchannel is parabolic. Since the fluid flow does not slip on the microchannel walls, the velocity in these areas is equal to zero and the maximum velocity occurs along the microchannel center-

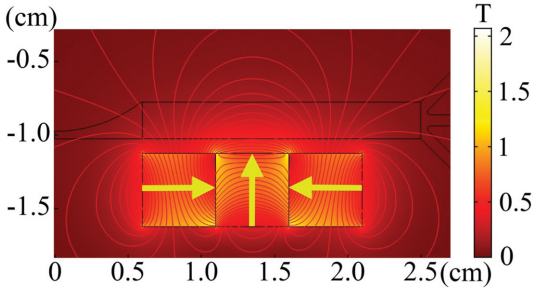


Fig. 13. The density distribution of the magnetic field for d=1 mm. The red lines indicate the induced magnetic field and the yellow arrows represent the direction of the magnetization.

line. The fluid flow velocity distribution along the x-axis in curved and straight sections of the microchannel is determined by using the simulation results at different inlet Reynolds numbers. It is normalized with the maximum velocity at the same cross section presented in Table 2. The results are in complete agreement with the ones reported by Ref. [23].

The distribution of the magnetic field is shown in Fig. 13 for the magnet with the distance of d=1 mm to the channel. Three permanent magnets with a Halbach arrangement were placed at different distances from the upper wall of the microchannel. This configuration extends the magnetic field on one side to farther distances. The red lines representing the distribution of the induced magnetic field in Fig. 13 confirm the extent of the magnetic field. In the Halbach arrangement, the polarization angles of the magnet rotate as much as 90°. The yellow arrows indicate the magnetizing direction of the magnets. The distribution of magnetic field flux density is amplified on the side of the magnet where the microchannel is located. It can be concluded that the Halbach array of magnets and their location in the vicinity of the proposed microchannel are appropriate choices. In the simulations, based on Eq. (9), the magnetizing direction of each magnet is determined according to the Halbach array of magnets shown in Fig. 13 as yellow arrows. The density of the induced magnetic field is higher

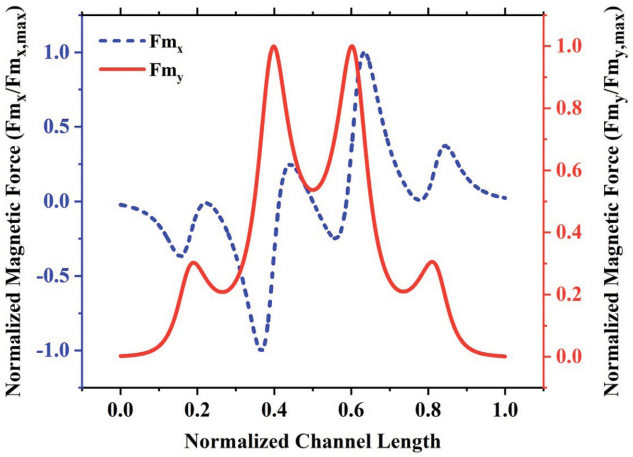


Fig. 14. Normalized components of the magnetophoretic force applied to the microparticles along the outer wall of the channel in the straight section.

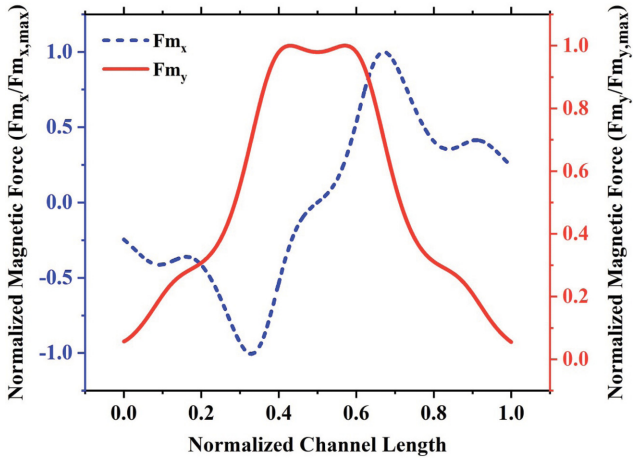


Fig. 15. Normalized components of the magnetophoretic force applied to the microparticles along the channel centerline in the straight section.

along the intersections of magnets compared to other parts of the computational domain, which is in agreement with the results of Ref. [9].

Figs. 14 and 15 demonstrate horizontal and vertical components of magnetophoretic force applied to microparticles for the Halbach array of magnets at d=1 mm. These forces are shown along the outer wall of the channel and its centerline in the straight section, respectively. The effect of the magnetic field on the curved section of the microchannel is approximately negligible (Fig. 13). Thus, the magnetophoretic force distribution is important only in the flow direction within the straight section of the microchannel. As shown in Eq. (11), the magnetophoretic force is proportional to the square gradient of the magnetic field strength $F_M \propto \nabla(H^2)$. The magnetophoretic force components in the flow direction and in the direction perpendicular to the flow are $F_{M,x} \propto \frac{\partial}{\partial x}(H^2)$ and $F_{M,y} \propto \frac{\partial}{\partial y}(H^2)$, respectively. The changes in the magnetophoretic force in the x and y directions are obtained on the lower wall and centerline of the straight section of the microchannel and are normalized with their maximum values. Since the particles used in this study are of the diamagnetic type are exposed to the magnetic field, they are driven towards the region with the lowest magnetic field strength. The magnetophoretic force in the x-direction is negative from the inlet of the straight section of the microchannel to x/L=0.5, where L is the length of the straight section of the microchannel. The negative force pushes the particles away from the area with the strongest magnetic field to the outside of the magnetic field. From x/L=0.5 to x=L, the magnetophoretic force is positive, leading to the move of the particles away from the magnets. The point with the highest amount of magnetophoretic force is close to the intersection of the magnets, where it forms two peaks. As the distance from the magnets increases, i.e., y is enhanced, these two peaks tend to the point x/L=0.5. This can be observed by comparing Figs. 14 and 15. Considering the y-component magnetophoretic force, it is demonstrated that the amount of force is always positive, so the particles move away from the magnets. As the dis-

tance from the magnets increases, the slope of the magnetophoretic force at the peaks decreases due to the reduction of the gradient of the magnetic field intensity H. Note that the present results are in agreement with the same results presented by previous studies [21,34,42].

Based on the above analysis, it is revealed that the maximum force is formed near the intersection of the magnets. As the distance from the magnets increases, the slope of the magnetophoretic force decreases along the microchannel.

As mentioned in the theory section, the necessary conditions for the inertial separation of particles are $Re_p>1$ and a/h>0.07. The ratio of particle diameter to microchannel height for 5-, 10-, and 15-μm particles is 0.025, 0.05, and 0.075, respectively. Thus, only 15-μm

Table 3. Particle Reynolds number for different channel Reynolds numbers and various particle sizes

Re	$Re_p\|_{a=5\,\mu m}$	$Re_p\|_{a=10\,\mu m}$	$Re_p\|_{a=15\,\mu m}$
90	0.11	0.45	1.01
100	0.12	0.50	1.12
110	0.14	0.55	1.24
120	0.15	0.60	1.35

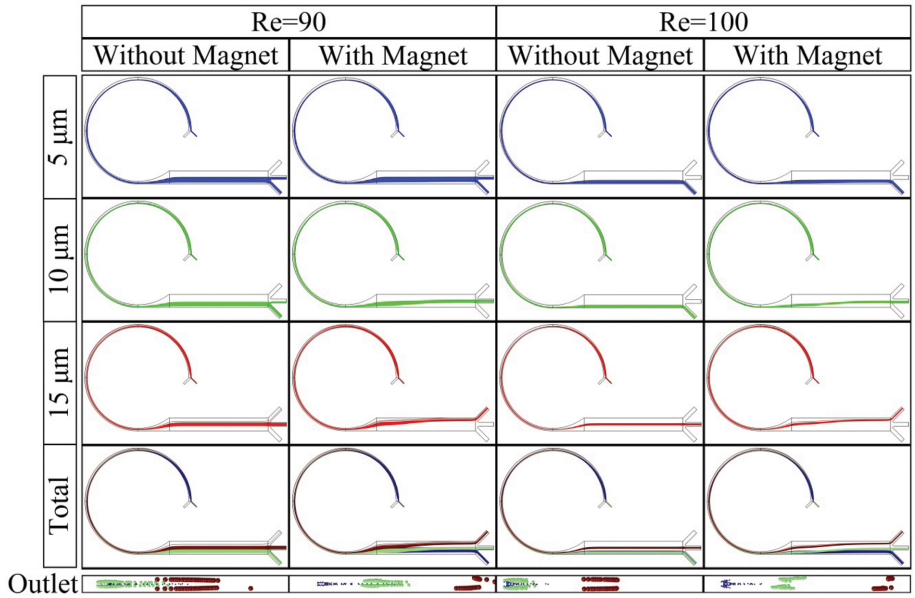


Fig. 16. The trajectory of different particles in the microchannel for Reynolds numbers of 90 and 100 in the presence and absence of magnetic field.

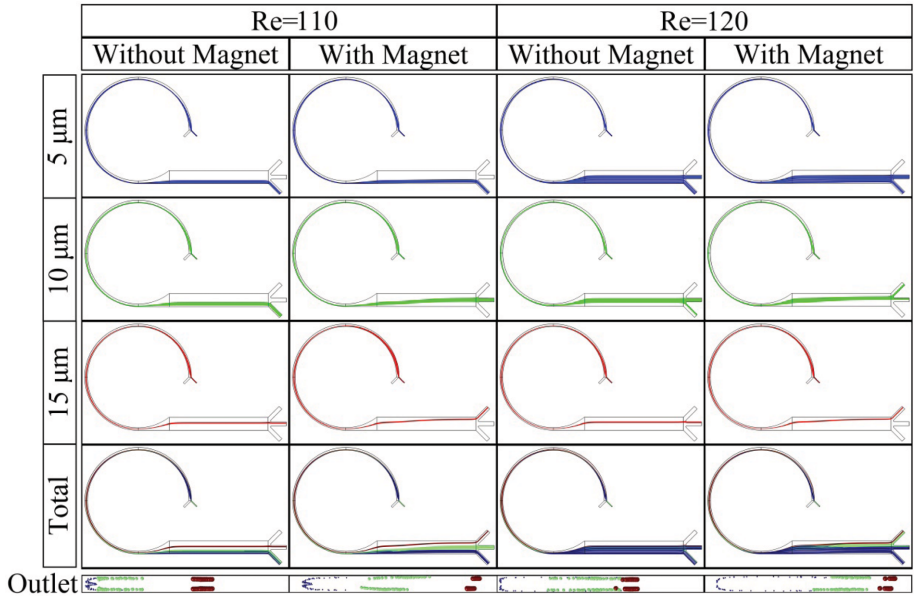


Fig. 17. The trajectory of different particles in the microchannel for Reynolds numbers of 110 and 120 in the presence and absence of magnetic field.

particles have the potential of inertial separation by the proposed microchannel. Now the particle Reynolds number should be calculated. Based on four Reynolds numbers of 90, 100, 110, and 120, the particle Reynolds number is calculated for 5-, 10-, and 15-μm particles (Table 3). As can be seen, Re_p>1 occurs just for 15-μm particles. Hence, 15-μm particles are expected to be separated using the proposed microchannel at Re≥90 without applying a magnetic field.

The trajectory of microparticles within the microchannel and the distribution of particles across the outlet of the microchannel are presented in Figs. 16 and 17 for four different Reynolds numbers when the Halbach array of magnets are positioned at a distance of 1 mm from the channel. The effect of the magnetic field on the trajectory of the particle is investigated in these figures by comparing the cases with and without the magnetic field. When the fluid flow passes through the curved part, lateral migration of 15-μm particles towards the outer channel wall occurs. This is because the inertial force overcomes the Dean drag force for these even without applying magnetic force. It is observed that 15-μm particles are separated from smaller ones and exit through the central outlet or the second one. As the flow velocity increases, the inertial focusing of 15-μm particles is enhanced so that they are completely separated from the other particles and exit through the second outlet at Re=100. For smaller particles, the Dean drag force

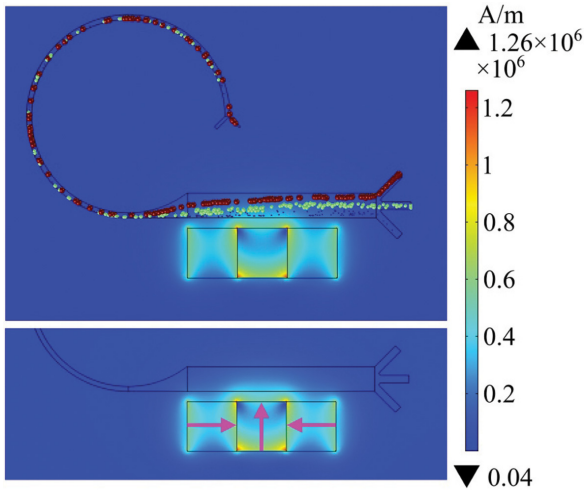


Fig. 18. Complete separation of three diamagnetic particles in the presence of magnetic field generated by three permanent magnets with a Halbach arrangement at Re=110. The color contour indicates the intensity of the magnetic field and the colored arrows show the magnetism of the magnets.

overcomes the inertial force, so the motion of these particles continues along with the Dean vortices so that the 5- and 10-μm par-

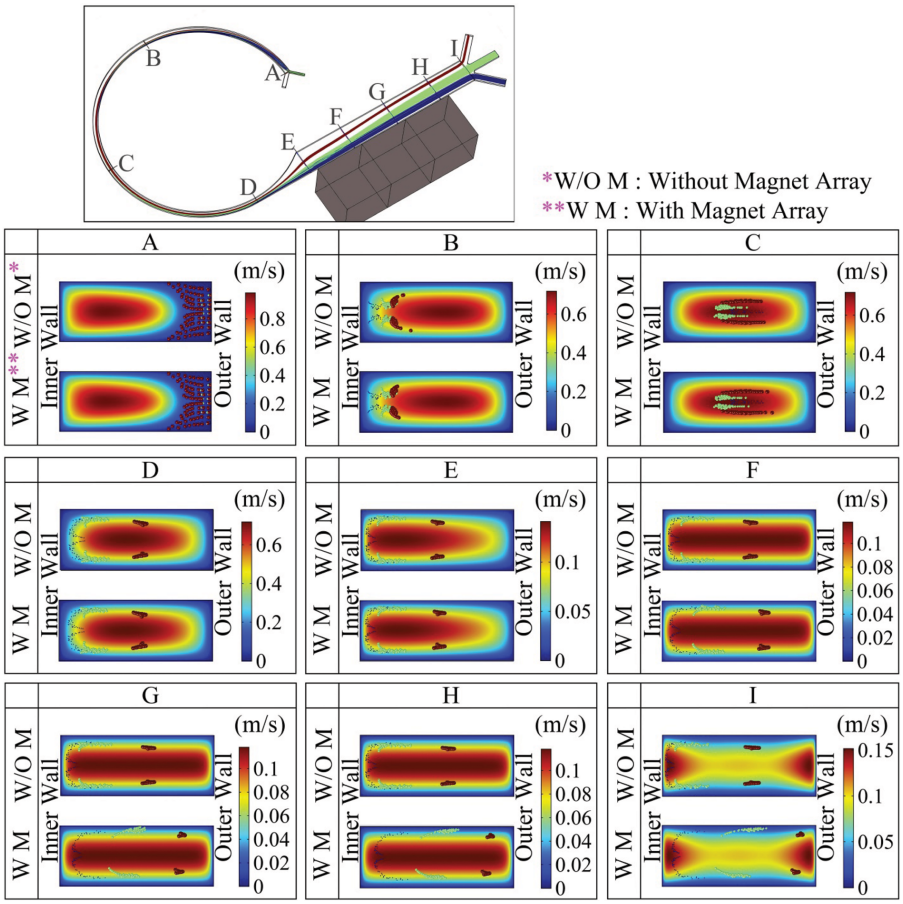


Fig. 19. Distribution of particles across different sections of the microchannel at Re=110 in the absence of the magnetic field compared to the Halbach arrangement at a distance of 1 mm from the channel.

ticles migrate towards the outer wall of the microchannel and exit through the second and third outlets without applying the magnetic force. When the magnetophoretic force is applied by placing the Halbach array of magnets at a distance of 1 mm from the microchannel, the particles migrate outward from the location of the magnets. As the magnetic field is applied at Reynolds numbers of 90 and 100, 15-μm particles deflect completely towards the first outlet. 10-μm particles are slightly deflected and migrate towards the second outlet in the presence of the magnetic field. However, this force is not enough for 5-μm particles to affect their lateral migration. It can be demonstrated that without applying a magnetic field, 15-μm particles are separated from smaller particles due to inertial force at Re=90 and 100. Besides, the magnetophoretic force can separate 5-μm from 10-μm particles at a Reynolds number of 100. Thus, all particles can be separated from each other under these circumstances.

The simulations were performed for Reynolds numbers of 110 and 120 and the results are presented in Fig. 17. It is shown that the results of Re=110 are similar to those of Re=100. As the flow rate increased, the 5- and 10-μm particles dispersed across the microchannel. Therefore, the optimal separation states occurred at Re=100 and 110. The separation of 15-μm particles occurred without the magnetic field, while the separation of two smaller particles occurred in the presence of the magnetic field. Fig. 18 shows a separation of selected particles in the presence of the magnetic field for three permanent magnets with Halbach arrangement at a distance of 1 mm from the microchannel.

Different cross sections of the channel and the distribution of particles in the presence and absence of the magnetic field are shown in Fig. 19 at Re=110. At the inlet of the channel (section A in Fig. 19), all particles are placed in the vicinity of the outer wall due to the sheath flow. It is shown that the effect of the magnetic field in the curved section is not considerable and the changes begin from section E. The microchannel is designed so that the negative magnetophoretic force causes the particles to move across the cross section of the microchannel and migrate from the vicinity of the outer

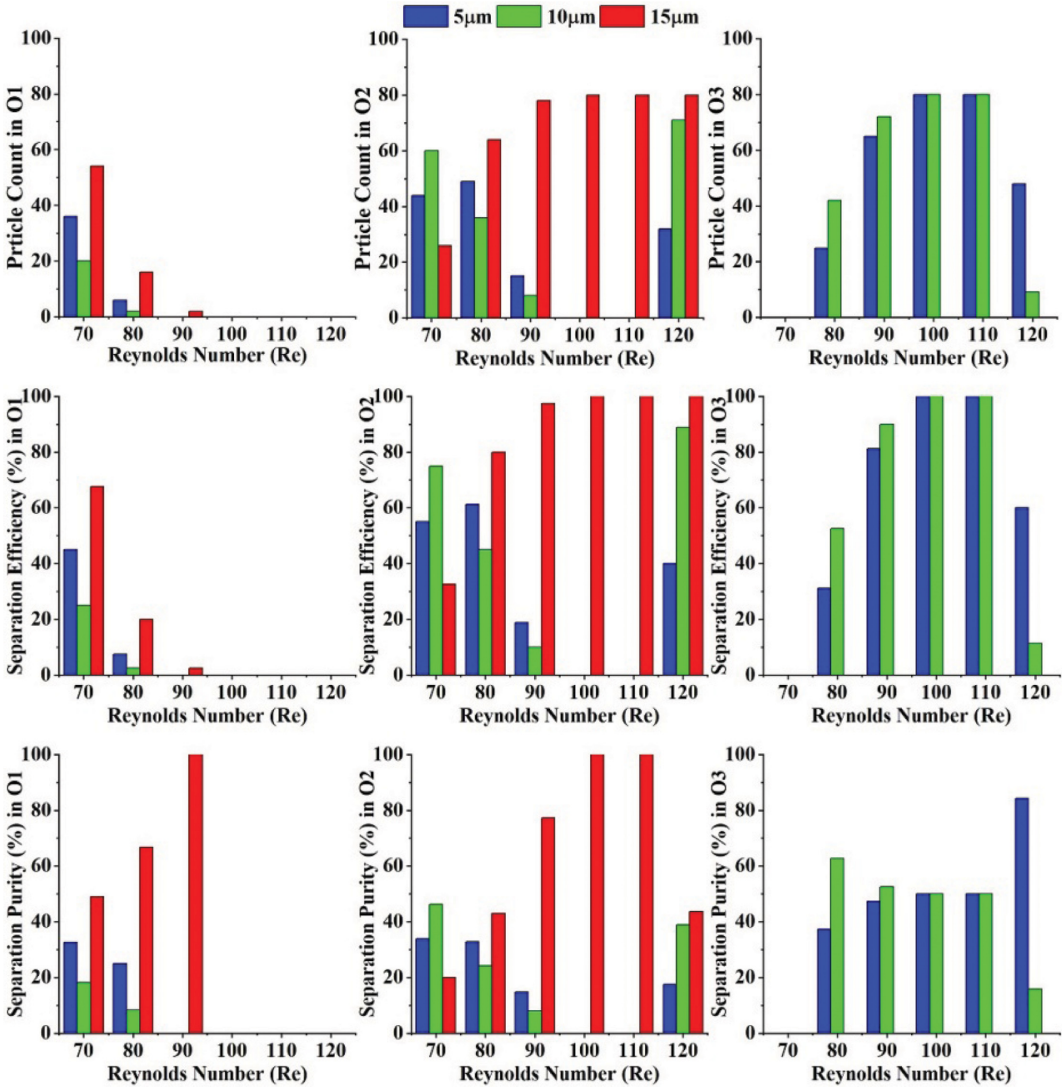


Fig. 20. Particle count at three microchannel outlets, separation efficiency, and purity for different Reynolds numbers in the absence of the magnetic field.

wall towards the inner wall. It should be pointed out that the channel width is displayed in all sections at the same time. The color contours in Fig. 10 represent the mainstream velocity. In the outlet section, i.e., section I in Fig. 19, the complete separation of 5-, 10- and 15-μm particles occurs.

2. Separation Efficiency and Purity

The most commonly used parameters to determine the performance of a microfluidic device are separation efficiency and purity. To achieve separation efficiency and purity, it is necessary to determine the number of particles separated in each outlet. Separation purity is the ratio of the number of target particles to the total output particles, and separation efficiency is the ratio of the number of target particles at an outlet to the total target particles at all outlets [90]. In experimental investigations, the most common method for counting and sizing particles is to collect samples from each outlet and then use the flow cytometry technique. In the numerical methods, particle counting is directly possible for each outlet. Fig. 20 shows the number of particles, the separation efficiency, and purity at each outlet without applying the magnetic field for different Reynolds numbers. Fig. 20 demonstrates that most 15-μm particles move towards the second outlet and most 5- and 10-μm particles exit from the third outlet in the absence of the magnetic field. The efficiency and purity of 15-micron particle separation in 100 and 110 Reynolds numbers is equal to 100%. Also, the separation efficiency of 5- and 10-μm particles at these two Reynolds numbers is equal to 100%, but their separation purity is equal to 50% due to the simultaneous exit of both particles from one outlet (second outlet), indicating inefficiency of the microfluidic device under these circumstances.

Fig. 21 shows the number of output particles, separation efficiency, and purity when the magnetophoretic force is generated due to the presence of the Halbach array of magnets at a distance of 1 mm from the channel. In this case, the tendency of 15-, 10-, and 5-μm particles is to pass through the first, second, and third outlets, respectively. By applying a magnetic field, the separation efficiency and purity of all three particles are increased so that under

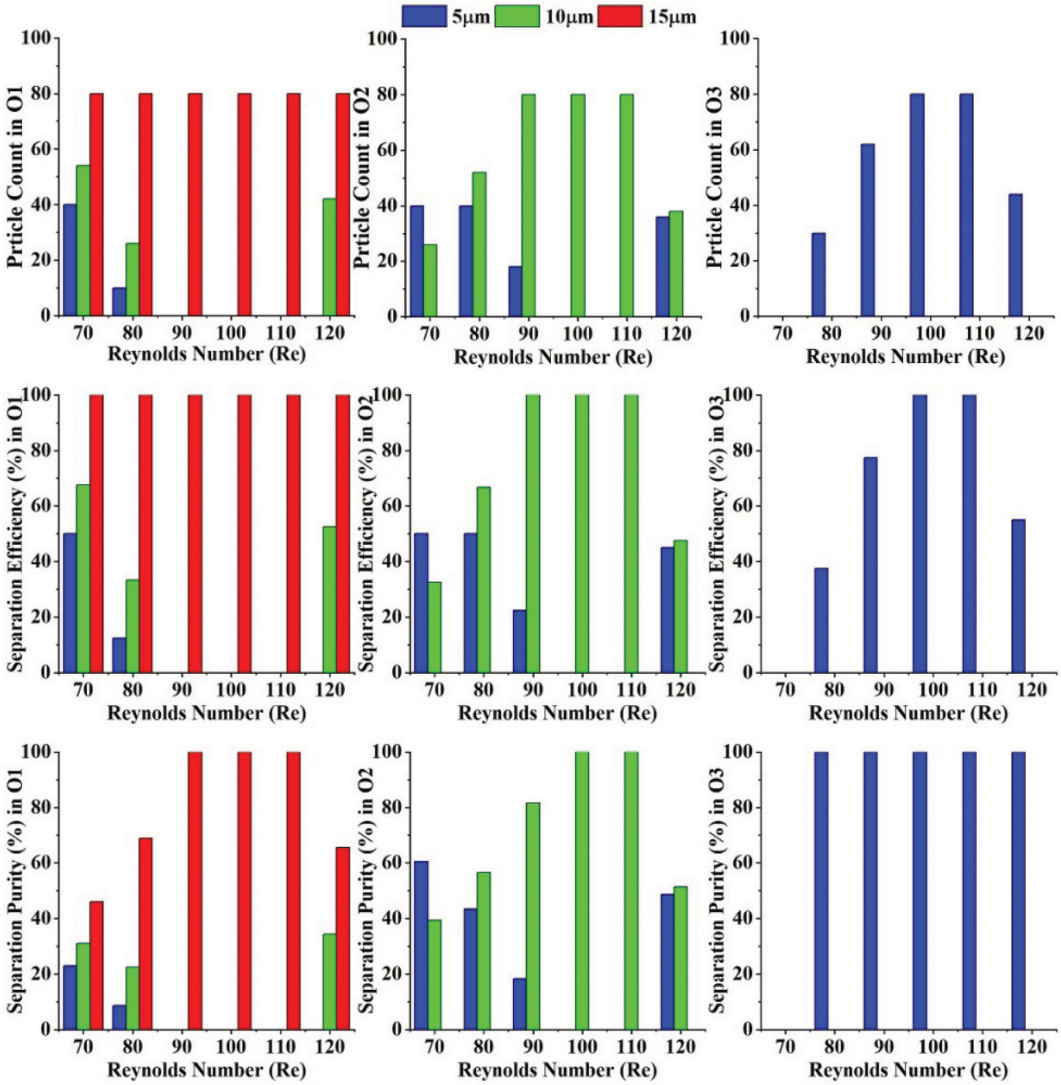


Fig. 21. Particle count at three microchannel outlets, separation efficiency, and purity for different Reynolds numbers when the magnetophoretic force is generated due to the presence of the Halbach array of magnets at a distance of 1 mm from the channel.

these conditions, the efficiency and purity of particles is 100% for the Reynolds numbers of 100 and 110. Therefore, 100% efficiency can be achieved using the proposed microfluidic device for the simultaneous separation of 5-, 10-, and 15-μm diamagnetic particles within a continuous ferrofluid flow.

3. The Effect of the Magnet Distance from the Microchannel

In this section, the effect of the Halbach array distance from the outer wall of the microchannel is studied. In this case, the Reynolds number is equal to 110 and simulations are performed for three different distances of the Halbach array from the microchannel as d=0.5 mm, d=1.5 mm, and d=2 mm. As mentioned, as the distance from the magnet increases, the intensity of the magnetic field decreases, resulting in a reduction in the magnetophoretic force. Fig. 22 presents the trajectory of particles for different distances of the Halbach array of magnets from the channel. For better comparison, the results for d=1 mm are also displayed. As the distance is reduced, the effect of the magnetophoretic force on the deflection of the particles decreases, leading to the repulsion of the 10-

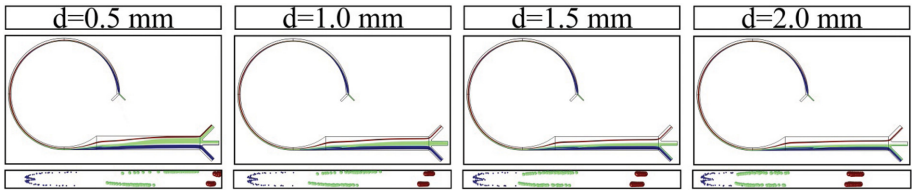


Fig. 22. The trajectory of different particles in the microchannel at Reynolds numbers of 110 and 120 in the presence and absence of magnets.

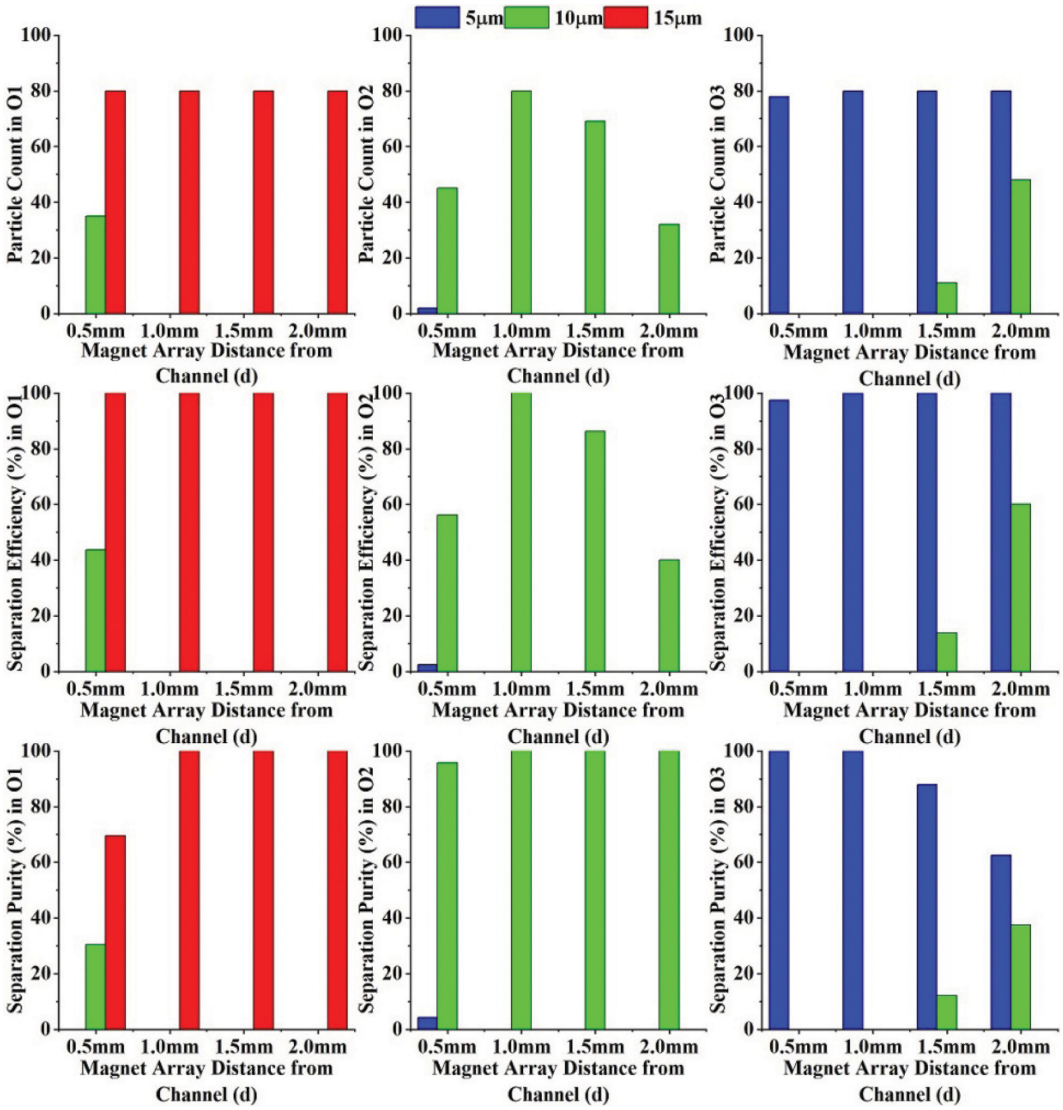


Fig. 23. Particle count at three microchannel outlets, separation efficiency, and purity for different distances of the Halbach array of magnets from the outer wall of the microchannel.

μm particles towards the inner wall, where the 15-μm particles are present.

The number of particles, separation efficiency, and purity of particles at each outlet are presented in Fig. 23 for different distances of Halbach array of magnets. It is revealed that the reduction of distance between the magnet array and the microchannel leads to an increase in the purity of 5-μm particles at third outlet. Besides, an increase in the distance results in an increase in particle separation purity of 10- and 15-μm particles and a reduction in the separation purity of 5-μm particles. It is shown that the distance of 1 mm between the magnets and the microchannel is the optimal case.

4. The Effect of the Number and Arrangement of Magnets

In this section, the effect of the number of magnets and their lateral position along the x-axis on the separation of particles is

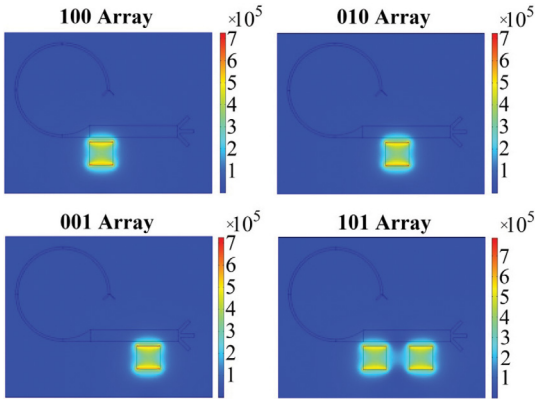


Fig. 24. Magnetic field strength contours for different positions of magnets.

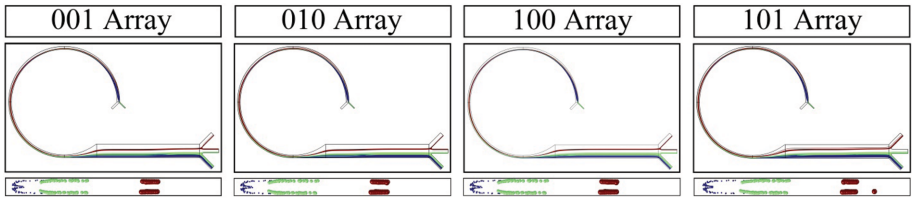


Fig. 25. The trajectory of different particles in the microchannel for different configurations of magnets at Re=110.

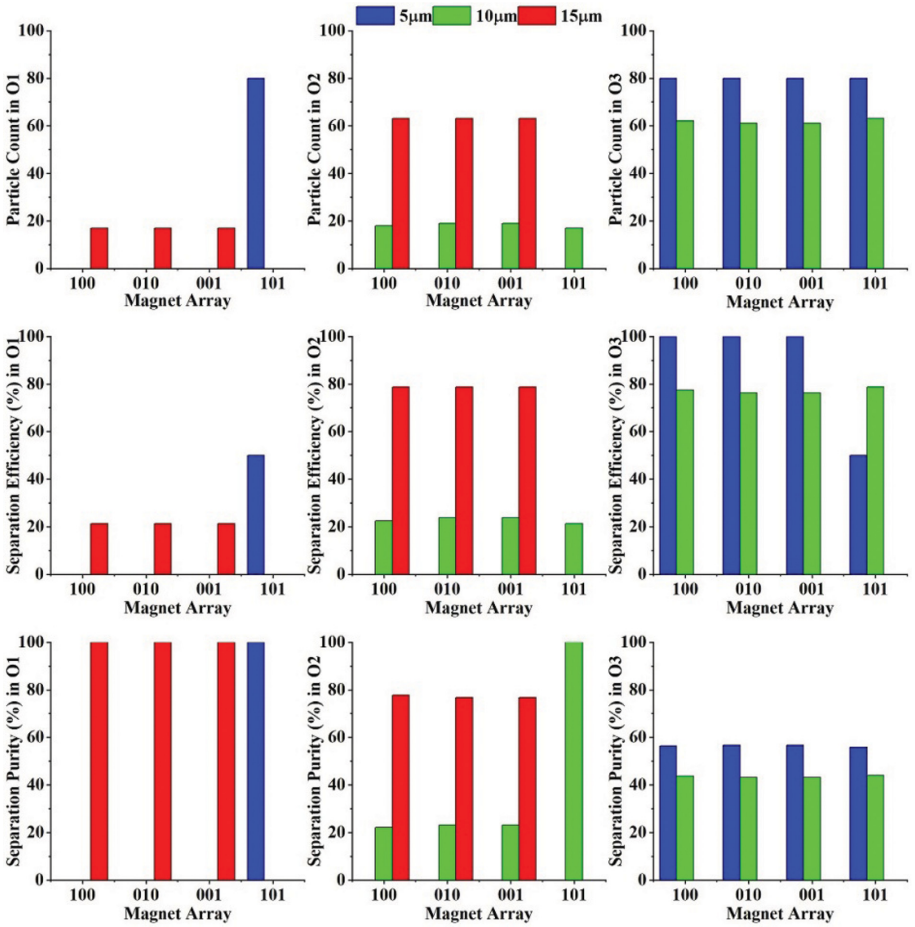


Fig. 26. Particle count at microchannel outlets, separation efficiency, and purity of particles for different magnet configurations.

evaluated to achieve the appropriate number and optimal arrangement of magnets. The Reynolds number is assumed to be constant (Re=100) and four different configurations called 100, 010, 001, and 101 are considered. Fig. 24 shows these arrangements and the intensity distribution of the magnetic field. The figure reveals that the maximum magnetic field strength for the introduced configurations is less than for the Halbach array of magnets that is 1.06×10^6 A/m.

Fig. 25 demonstrates that the above configurations do not have a significant effect on particle trajectory and only as the magnets approach the outlet of the spiral section; several 15-μm particles migrate towards the inner outlet of the microchannel under the negative magnetophoretic force induced by the magnets. Fig. 26 presents the separation efficiency and purity of particles for these configurations. This figure shows that the effect of reducing the magnetophoretic force by reducing the number of magnets leads to no deflection and manipulation of 5- and 10-μm particles that exit from the spiral part of the channel. As can be seen, a high percentage of these particles exit from the outer outlet (third outlet). Hence, it can be concluded that the Halbach array of three magnets is an optimal configuration to achieve complete separation of the three microparticles using the proposed microfluidic device.

CONCLUSIONS

In the present study, microfluidic separation of three types of diamagnetic particles suspended in a ferrofluid was performed by applying inertial and magnetophoretic forces using a novel microfluidic device. The proposed device consists of a spiral section for inertial focusing of particles and a straight channel for applying a magnetic field. The required magnetic field is obtained by placing three permanent neodymium magnets adjacent to the straight part of the microchannel. We used the Halbach array of magnets to strengthen the magnetic field. Three-dimensional numerical simulations were performed using CAMSOL Multiphysics 5.5 software to solve the governing equations. Simulations were performed for Reynolds numbers in the range of 70 to 120 to determine the optimal conditions in which the separation efficiency is maximum. Also, the effect of distance between magnets, their number, and configuration on particle separation was studied. For instance, 15-μm particles were separated from smaller particles without applying a magnetic field due to inertial force at Re=90 and 100. The magnetophoretic force can separate 5-μm from 10-μm particles at a Reynolds number of 100. Thus, all particles can be separated from each other using the combination of inertial focusing and magnetophoretic force. The results demonstrate that the proposed device provides complete separation of 5-, 10-, and 15-μm particles for the Reynolds numbers of 110-100 using Halbach array of magnets at a distance of 1 mm from the outer wall of the microchannel. The proposed microfluidic device is very easily industrially fabricated for biomedical applications. In the future, the proposed microdevice can be modified for the separation of smaller microparticles, for example, 2-μm particles. Moreover, the deformability of particles may be considered when inertial and magnetophoretic forces are applied.

CONFLICT OF INTEREST

The authors declare that they have no conflict of interest.

REFERENCES

1. P. Sajeesh and A. K. Sen, *Microfluid Nanofluidics*, **17**, 1 (2014).
2. M. Bayareh, *Chem. Eng. Process.*, **153**, 107984 (2020).
3. Y.-Y. Chiu, C.-K. Huang and Y.-W. Lu, *Biomicrofluidics*, **10**, 011906 (2016).
4. T. S. Tran, B. D. Ho, J. P. Beech and J. O. Tegenfeldt, *Lab on a Chip*, **17**, 3592 (2017).
5. M. Yamada, M. Nakashima and M. Seki, *Anal. Chem.*, **76**(18), 5465 (2004).
6. S. S. Kuntaegowdanahalli, A. A. S. Bhagat, G. Kumar and I. Papautsky, *Lab on a Chip*, **9**, 2973 (2009).
7. I. Doh and Y.-H. Cho, S*ens. Actuators A*, **121**, 59 (2005).
8. D. Baresch, J.-L. Thomas and R. Marchiano, *Phys. Rev. Lett.*, **116**, 024301 (2016).
9. A. Abdulla, W. Liu, A. Gholamipour-Shirazi, J. Sun and X. Ding, *Anal. Chem.*, **90**, 4397 (2018).
10. Y. Zhou, Z. Ma and Y. Ai, *Microsyst. Nanoeng.*, **4**, 1 (2018).
11. D. Di Carlo, D. Irimia, R. G. Tompkins and M. Toner, *Proc. Natl. Acad. Sci.*, **104**, 18892 (2007).
12. S. Dutz, M. E. Hayden, A. Schaap, B. Stoeber and U. O. Hafeli, *J. Magn. Magn. Mater.*, **324**, 3791 (2012).
13. A. Russom, A. K. Gupta, S. Nagrath, D. Di Carlo, J. F. Edd and M. Toner, *New J. Phys.*, **11**, 075025 (2009).
14. J. M. Martel and M. Toner, *Annu. Rev. Biomed. Eng.*, **16**, 371 (2014).
15. A. A. S. Bhagat, S. S. Kuntaegowdanahalli and I. Papautsky, *Lab on a Chip*, **8**, 1906 (2008).
16. A. Al-Halhouli, W. Al-Fagheri, B. Alhamarneh, L. Hecht and A. Dietzel, *Micromachines*, **9**, 171 (2018).
17. J. Sun, M. Li, C. Liu, Y. Zhang, D. Liu, W. Liu, G. Hu and X. Jiang, *Lab on a Chip*, **12**, 3952 (2012).
18. P. Yeh, Z. Dai, M. Bergeron, Z. Zhang, M. Lin and X. Cao, *Sens. Actuators B Chem.*, **252**, 606 (2017).
19. A. S. Rzhevskiy, S. R. Bazaz, L. Ding, A. Kapitannikova, N. Sayyadi, D. Campbell, B. Walsh, D. Gillatt, M. Ebrahimi Warkiani and A. V. Zvyagin, *Cancers*, **12**, 81 (2020).
20. A. Munaz, M. J. Shiddiky and N.-T. Nguyen, *Biomicrofluidics*, **12**, 031501 (2018).
21. A. Munaz, M. J. Shiddiky and N.-T. Nguyen, *Sens. Actuators B Chem.*, **275**, 459 (2018).
22. T. Zhu, R. Cheng, S. A. Lee, E. Rajaraman, M. A. Eiteman, T. D. Querec, E. R. Unger and L. Mao, *Microfluidic Nanofluidics*, **13**, 645 (2012).
23. J. Zhang, S. Yan, D. Yuan, Q. Zhao, S. H. Tan, N.-T Nguyen and W. Li, *Lab on a Chip*, **16**, 3947 (2016).
24. W. Zhao, R. Cheng, S. H. Lim, J. R. Miller, W. Zhang, W. Tang, J. Xie and L. Mao, *Lab Chip*, **17**, 2243 (2017).
25. J. Wu, Y. Cui, S. Xuan and X. Gong, *Microfluidic Nanofluidics*, **22**, 103 (2018).
26. M. Xue, A. Xiang, Y. Guo, L. Wang, W. Wang, G. Ji and Z. Lu, *RSC Adv.*, **9**, 38496 (2019).
27. S. Ookawara, D. Street and K. Ogawa, *Chem. Eng. Sci.*, **61**, 3714

(2006).
28. X. Han, Y. Feng, Q. Cao and L. Li, *Microfluidic Nanofluidics*, **18**, 1209 (2015).
29. M. E. Warkiani, A. K. P. Tay, G. Guan and J. Han, *Sci. Rep.*, **5**, 11018 (2015).
30. J. M. Martel and M. Toner, *Phys. Fluids*, **24**, 032001 (2012).
31. D. Y. Kim and J. M. Kim, *Korean J. Chem. Eng.*, **36**, 837 (2019).
32. A. Thanormsridetchai, D. Ketpun, W. Srituravanich, P. Piyaviriyakul, A. Sailasuta, W. Jeamsaksiri, W. Sripumkhai and A. Pimpin, *J. Mech. Sci. Technol.*, **31**, 5397 (2017).
33. A. Özbey, M. Karimzadehkhouei, S. Akgonul, D. Gozuacik and A. Kosar, *Sci. Rep.*, **6**, 38809 (2016).
34. A. Shiriny and M. Bayareh, *Meccanica*, **55**, 1903 (2020).
35. J. Vanderlinde, *Classical electromagnetic theory*, Springer, Netherland (2006).
36. S.-E. K. Fateen and M. Magdy, *Chem. Eng. Res. Des.*, **95**, 69 (2015).
37. R. Cheng, T. Zhu and L. Mao, *Microfluidic Nanofluidics*, **16**, 1143 (2014).
38. Y. Zhou, D. T. Kumar, A. Kale, J. DuBose, Y. Song, J. Wang, D. Li and X. Xuan, *Biomicrofluidics*, **9**, 044102 (2015).
39. Q. Chen, D. Li, J. Lin, M. Wang and X. Xuan, *Anal. Chem.*, **89**, 6915 (2017).
40. A. Shiriny and M. Bayareh, *Chem. Eng. Sci.*, **229**, 116102 (2021).
41. H. W. Hou, M. Ebrahimi Warkiani, B. L. Khoo, Z. R. Li, R. A. Soo, D. S.-W. Tan, W. T. Lim, J. Han, A. A. S. Bhagat and C. T. Lim, *Sci. Rep.*, **3**, 1259 (2013).
42. Y. He, L. Luo and S. Huang, *Int. J. Mod. Phys. B*, **33**, 1950047 (2019).